

# Depth Optimization of Ansatz Circuits for Variational Quantum Algorithms

Spyros Tserkis,<sup>1,2,\*</sup> Muhammad Umer,<sup>3,†</sup> and Dimitris G. Angelakis<sup>4,2,3,‡</sup>

<sup>1</sup>*School of Electrical and Computer Engineering, Technical University of Crete, Chania 73100, Greece*

<sup>2</sup>*Institute for Quantum Computing and Quantum Technologies, NCSR Demokritos, Greece*

<sup>3</sup>*Centre for Quantum Technologies, National University of Singapore, 3 Science Drive 2, 117543, Singapore*

<sup>4</sup>*School of Electronics and Computer Science, University of Southampton, Southampton SO17 1BJ, UK*

The increasing depth of quantum circuits presents a major limitation for the execution of quantum algorithms, as the limited coherence time of physical qubits leads to noise that manifests as errors during computation. In this work, we focus on circuits relevant to variational quantum algorithms and demonstrate that their depth can be reduced by introducing additional qubits, mid-circuit measurements, and classically controlled operations. As an illustrative example, we consider nonlinear dynamics governed by the one-dimensional Burgers' equation, which has broad applications in computational fluid dynamics. In particular, we show that the proposed non-unitary quantum circuits can efficiently represent fluid flow configurations in both laminar and turbulent regimes. Furthermore, we demonstrate that, when noise is taken into account, these circuits are advantageous in regimes where two-qubit gate error rates are relatively low compared to idling error rates.

## I. INTRODUCTION

Implementing quantum algorithms often requires circuits with considerable depth, especially as the complexity of the computational task increases. These deep circuits typically involve highly entangled states that must retain coherence for extended durations, which presents a major challenge for current quantum hardware. Consequently, reducing circuit depth has become a central goal in quantum algorithm design, and a substantial body of research has been dedicated to this problem. In particular, shallower circuits can be achieved either by optimizing the gate sequence applied to existing qubits [1–6] or by increasing the number of qubits, which in turn often requires the use of mid-circuit measurements and classically controlled operations [7–16].

In this work, we adopt the latter approach for circuits relevant to variational quantum algorithms, and show how a unitary circuit can be replaced by a shallower non-unitary circuit that effectively induces the same transformation. The core idea of our method is to substitute two qubit gates with equivalent non-unitary processes that yields the same effect on the relevant qubits. Gate teleportation [17, 18], a well-known protocol in quantum information, is conceptually based on the same idea, as it employs extra qubits, measurements, and classically controlled operations to simulate a unitary gate.

In our analysis, we model the limited coherence of physical qubits as idling noise incurred during periods without active operations and show that this noise can be mitigated by reducing the two-qubit gate depth of the circuit. We also discuss the main limitation of our approach, namely its reliance on the circuit structure of the underlying unitary process. However, this restriction is not severe, as most variational quantum algorithms naturally conform to circuit architectures to which our method can be applied. As a concrete illustration, we present an example from the field of computational fluid dynamics.

The remainder of the paper is structured as follows. In Section II the method of rewriting the unitary ansatz circuits into non-unitary ones is presented, alongside a brief discussion on the relevance of those circuits on variational quantum algorithms. In Section III the noise model is presented alongside the error budget for three particular circuits. In Section IV an analysis of the main results of the paper is given, where the non-unitary circuits are compared with the conventional unitary ones. Finally the paper is concluded in Section V.

## II. OPTIMIZING ANSATZ CIRCUITS

Variational quantum algorithms (VQAs) [19, 20] rely on parameterized quantum circuits, known as *ansatz* circuits, designed to prepare quantum states that approximate the solution to a given problem. These circuits typically consist of alternating layers of single qubit rotations and entangling two-qubit gates, with the parameters updated iteratively by a classical optimizer to minimize a cost function dependent on the problem. The structure of the ansatz plays a crucial role in the performance of the algorithm, as it must be expressive enough [21] to represent the target state while remaining shall-

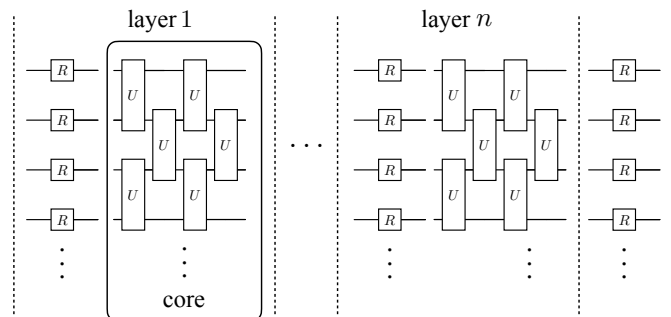


FIG. 1. Generic ansatz circuit used in VQAs. The circuit consists of multiple layers, each starting with a random rotation on each qubit and a core circuit where two qubit gates can be added in different formations. At the end, another layer of rotations is added.

\* [spyrostserkis@gmail.com](mailto:spyrostserkis@gmail.com)

† [umer@u.nus.edu](mailto:umer@u.nus.edu)

‡ [dimitris.angelakis@gmail.com](mailto:dimitris.angelakis@gmail.com)

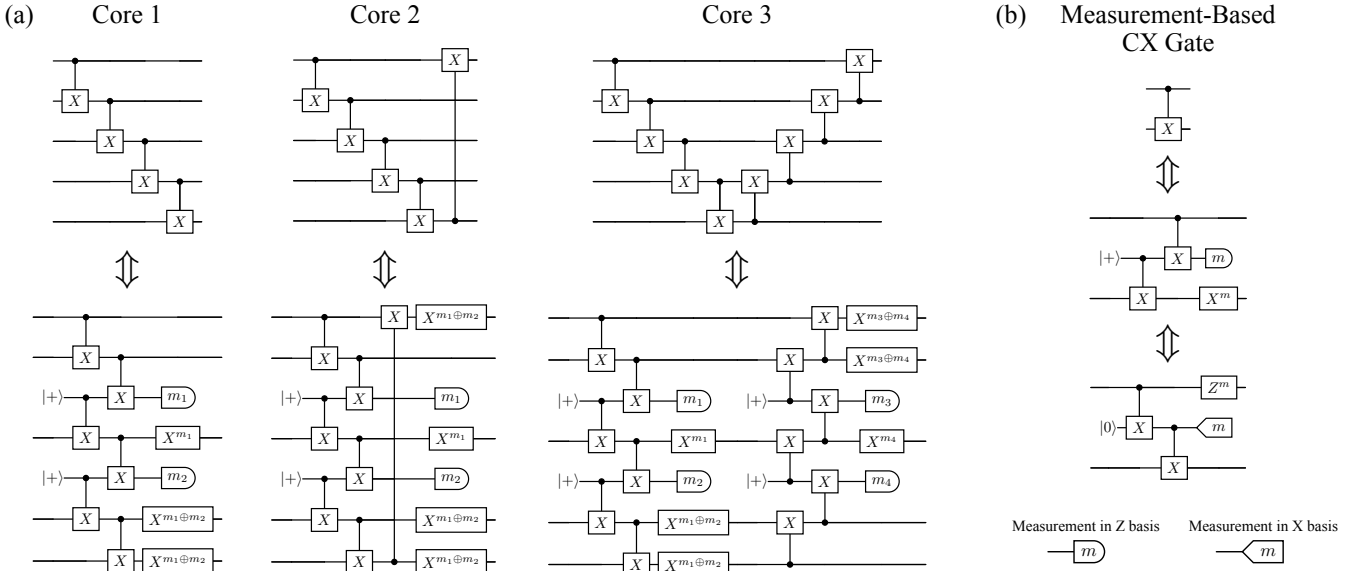


FIG. 2. In panel (a) three core circuits are depicted in a unitary (top) and a non-unitary (bottom) structure. The circuits provide an equivalent transformation on the register qubits. In panel (b) the measurement-based CX gate is depicted in two equivalent ways, which helps depending on the type of circuit that is under investigation.

low enough to be implementable on current or near-term hardware. A generic ansatz circuit illustrating this layered structure is shown in Figure 1. The entangling two-qubit gates are typically controlled-X (CX) gates, which can be arranged in different configurations. We refer to the part of each layer that corresponds to this formation as *core* circuit, and is the one whose depth will be optimized in our analysis below.

The top side of Figure 2(a) shows three such core circuits that can be found useful in recent literature [21–23]. It is evident from the core structures that as the number of qubits, namely the width of a circuit, increases, the two-qubit gate depth grows linearly. Specifically, for a circuit width equal to  $n$ , the two-qubit gate depth of core 1 is  $n - 1$ , that of core 2 is  $n$ , and that of core 3 is  $2(n - 1)$ . This linear relation between width and depth leads to quite long circuits that need to maintain coherence for an extended period of time, a requirement that is beyond current technology capabilities. In what follows, we show how the depth of those circuits can be reduced, suppressing at the same time the idling errors induced during periods of time that no other operation is applied on the qubits.

Before we get into depth reduction of the core circuits, let us introduce the premise of this method. It is a particular substitution of the CX gate with its measurement-based equivalent circuit, shown in Figure 2(b). More specifically apart from the two register qubits, an extra qubit is added, called auxiliary, initialized to a particular fixed state, e.g.,  $|0\rangle$  or  $|+\rangle$ . The auxiliary qubit interacts with both of the register qubits introducing entanglement in the circuit, and is subsequently measured on a particular basis depending on the construction. Based on the measurement outcome, a conditional gate is applied. The total effect of the circuit realizes the CX gate on the register qubits. The equivalence between the unitary and the

measurement-based versions of the CX gate is a result that has been mentioned before in the literature [24], but it has not been previously applied in the context of VQAs to reduce circuit depth. For completeness sake a proof of this equivalence is provided in Appendix A. Analogous constructions can easily be found for an arbitrary controlled-U (CU) gate, but the point of this work is to focus on quantum computing gates rather than arbitrary unitary transformations. This measurement-based operation is reminiscent of the gate teleportation protocol [17, 18], with the key distinction that the latter requires two auxiliary qubits which are initialized in an entangled state. In practice, starting with a CX gate, if we substitute the primitive circuit shown in Figure 2(b) twice, we retrieve a teleported CX gate.

In this paper, we focus on core circuits constructed via a series of CX gates where one starts at the point the previous ends forming a structure we refer to as *ladder*, as shown at the top of Figure 2(a) for the case of five qubits.<sup>1</sup> Then, we can substitute each CX gate with its measurement-based equivalent in a completely modular manner, as shown at the bottom of Figure 2(a). Given the modularity of this technique the circuit width is irrelevant as long as the ladder structure is maintained. In practice, the first and last CX gates of the unitary circuit do not need to be substituted, thereby reducing the total number of auxiliary qubits, measurements, and conditional gates. In Appendix B we show diagrammatically how core 1 was transformed from a unitary to a non-unitary circuit step by step. In Appendix C we also provide a different construction for the non-unitary circuit of core 3, where all measurements

<sup>1</sup> In the case of core 2, the first and last qubits can be thought of as physically adjacent if the qubits are placed in a cyclic arrangement.

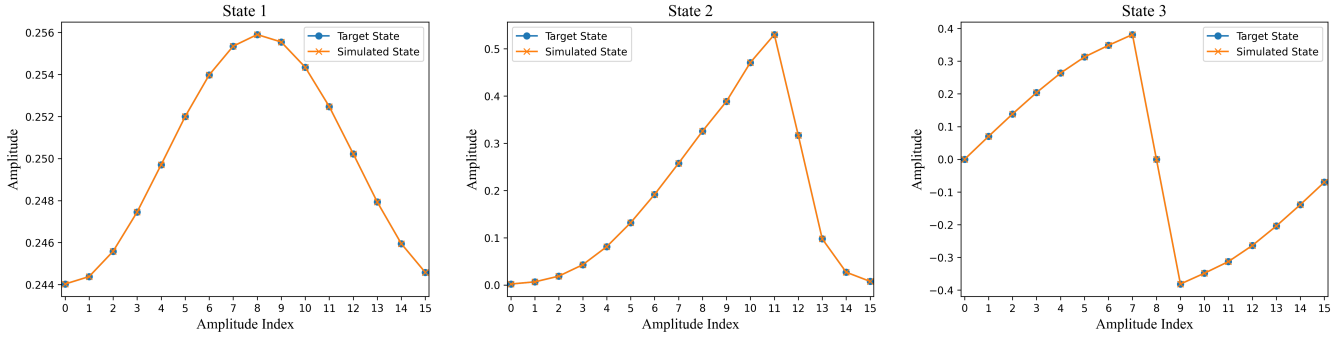


FIG. 3. Simulation of three time-evolved states corresponding to the one-dimensional Burgers' equation using four qubits. The x-axis corresponds to the amplitude index, where index 0 represents the amplitude of  $|0000\rangle$ , index 1 represents the amplitude of  $|0001\rangle$ , and so on, while the y-axis corresponds to the amplitude value. State 1 is the time-evolved Gaussian state ( $t = 0.083$ ) with kinematic viscosity coefficient set to the laminar flow regime ( $\nu = 10$ ). State 2 is the time-evolved Gaussian state ( $t = 0.83$ ) with kinematic viscosity coefficient set to the turbulent flow regime ( $\nu = 10^{-3}$ ). State 3 is the time-evolved sinusoidal ( $t = 0.83$ ) with kinematic viscosity coefficient set to the turbulent flow regime ( $\nu = 10^{-3}$ ). An ansatz circuit based on non-unitary core circuit 1 was used for all simulated states with five layers. The infidelities reached for each state were  $1.5\text{e-}13$ ,  $2.1\text{e-}13$ , and  $5.2\text{-}14$ , respectively from left to right.

have been commuted at the end, commenting its potential advantages and disadvantages.

The technique proposed in this work effectively increases the width and two-qubit gate density of a circuit by reducing its depth. As a result, depth reduction is not feasible for circuits that are already too dense in terms of two-qubit gates, such as the one shown in Figure 1. However, ladder type ansatz circuits, which feature sparser two qubit connectivity, are common in the literature. This makes the proposed optimization method applicable to a large portion of VQA implementations. Note that the trade-off between circuit width and depth can also be understood in terms of the active and idle volume discussed in Ref. [25]. In particular, the largest part of the circuit volume in the unitary core circuits at the top of Figure 2(a) consists of idle volume, whereas the largest part of the circuit volume in the non-unitary core circuits at the bottom of Figure 2(a) consists of active volume.

Let us now show how an ansatz circuit based on the non-unitary version of core 1 can indeed construct states relevant to a problem approached through VQA. In particular, we consider the nonlinear dynamics governed by the one-dimensional viscous Burgers' equation

$$\partial_t u(x, t) = [\nu \partial_x^2 - u(x, t) \partial_x] u(x, t). \quad (1)$$

The wavefunction  $u(x, t)$  represents the real-valued fluid field. The first term on the right-hand side of the equation corresponds to diffusion and the second term to convection, where  $\nu$  denotes the kinematic viscosity coefficient that governs the regime of fluid flow and determines the transition between laminar and turbulent behavior. The solution of this differential equation for each point  $x_i$ , i.e.,  $u(x_i, t)$ , can be numerically found given an initial wavefunction and a specific value for the parameter  $\nu$ .

The nonlinear Burgers' dynamics can also be variationally resolved [23, 26] by training an ansatz circuit with  $n$  register qubits to produce a simulated state  $|u(t)\rangle$  whose  $2^n$  amplitudes  $u(t)_i$  correspond to the solution of the differential equa-

tion (1), i.e.,

$$|u(t)\rangle = \sum_{i=0}^{2^n-1} u(t)_i |i\rangle = \sum_{i=0}^{2^n-1} u(x_i, t) |i\rangle, \quad (2)$$

where  $|i\rangle = |b_3(i)b_2(i)b_1(i)b_0(i)\rangle = |\text{bin}_4(i)\rangle$ , with  $b_k(i) = \lfloor \frac{i}{2^k} \rfloor \bmod 2$ , e.g.  $|0\rangle = |0000\rangle$ ,  $|1\rangle = |0001\rangle$ , etc.

The input state of the ansatz circuit is  $\sum_{i=0}^{2^n-1} |0\rangle$ . The output, i.e., simulated, state is constructed by variationally changing the rotation angles of the ansatz circuit. Our goal is to keep changing the rotation angles until the simulated state gets as close as possible to the target state. In order to achieve that we optimize a cost function for each set of rotation angles. In particular we minimize the infidelity  $1 - F_{\text{st}}$  between the target and simulated state, where  $F_{\text{st}}$  is the Uhlmann-Jozsa state fidelity [27, 28].

We consider three cases shown in Figure 3(a), (b), and (c), respectively. In the first case, the initial state is Gaussian with viscosity  $\nu = 10$  (laminar flow). In the second case, the initial state is Gaussian with viscosity  $\nu = 10^{-3}$  (turbulent flow), and in the third case, the initial state is sinusoidal with viscosity  $\nu = 10^{-3}$  (turbulent flow). We solve the differential equation (1) and obtain the time-evolved states at  $t = 0.083$  for the first case and  $t = 0.83$  for the remaining two. Table II in Appendix D presents the infidelities of the three target states for up to five layers. In Figure 3 only the simulated states with five layers are shown, corresponding to the best approximations within this range. Note that the simulations do not include noise, as they are intended solely to demonstrate convergence to the target states under ideal conditions. If noise were taken into account, the infidelities would increase, indicating a departure from the target states. The results are practically identical to those obtained using unitary ansatz circuits, since in the absence of noise both approaches yield equivalent outcomes.

TABLE I. Error budget characteristics of both unitary and non-unitary circuits for core circuits 1, 2, and 3. In particular, for each core circuit the following parameters are shown in terms of circuit depth  $n$ : type of circuit, CX depth, the idling time steps  $t_{\text{idle}}$ , the number of CX gates  $n_{\text{CX}}$ , the number of measurements  $n_{\text{meas}}$ , the number of qubit initializations  $n_{\text{in}}$ , and the number of conditional single-qubit gates  $n_{\text{con}}$ .

Circuit	Type	CX depth	$t_{\text{idle}}$	$n_{\text{CX}}$	$n_{\text{meas}}$	$n_{\text{in}}$	$n_{\text{con}}$
Core 1	Unitary	$n - 1$	$n^2 - 3n + 2$	$n - 1$	0	0	0
	Non-unitary	2	4	$2n - 4$	$n - 3$	$n - 3$	$n - 2$
Core 2	Unitary	$n$	$n^2 - 2n$	$n$	0	0	0
	Non-unitary	2	$2n - 2$	$2n - 3$	$n - 3$	$n - 3$	$n - 2$
Core 3	Unitary	$2n - 2$	$2n^2 - 6n + 4$	$2n - 2$	0	0	0
	Non-unitary	4	$n + 8$	$4n - 8$	$2n - 6$	$2n - 6$	$2n - 4$

### III. NOISE MODEL AND BENCHMARKING

The noise model we follow in this work is based on the one presented in Ref. [29]. Given a quantum state with density matrix  $S$ , the noisy process is represented by a Pauli quantum channel  $\Lambda(S)$  as follows

$$\Lambda(S) = (1 - p)S + pPSP^\dagger, \quad (3)$$

where  $P$  belongs to the Pauli group  $\mathbb{P}$ , and  $p = \frac{1-e^{-2\lambda}}{2}$  is the error probability with  $\lambda \in \mathbb{R}^+$ . This noise model assumes that a twirling approximation has been applied to remove non-Pauli noise, which is typical for error analysis in quantum computing even though in real quantum computers non-Pauli noise is also expected to be present.

Given the twirling approximation, all noise elements, e.g., X gates corresponding to bit-flips or Z gates corresponding to phase-flips etc., can be commuted to the very end of the circuit, allowing us to more easily approximate its total impact. In order to do so, and following the analysis of Ref. [14], all the errors occurred throughout the circuit can be aggregated in a total decoherence parameter  $\lambda_{\text{tot}}$  as follows:

$$\lambda_{\text{tot}} = t_{\text{idle}}\lambda_{\text{idle}} + n_{\text{CX}}\lambda_{\text{CX}} + n_{\text{meas}}\lambda_{\text{meas}} + n_{\text{in}}\lambda_{\text{in}} + n_{\text{con}}\lambda_{\text{con}}. \quad (4)$$

In the above expression,  $t_{\text{idle}}$  corresponds to the time-steps where coherence needs to be maintained for quantum states while no other operation is implemented. The decoherence per idle time-step is associated to the parameter  $\lambda_{\text{idle}}$ . The total number of CX gates is given by  $n_{\text{CX}}$  and the corresponding decoherence with  $\lambda_{\text{CX}}$ . Analogously we have  $n_{\text{meas}}$  and  $\lambda_{\text{meas}}$  for the mid-measurements,  $n_{\text{in}}$  and  $\lambda_{\text{in}}$  for qubit initialization, and  $n_{\text{con}}$  and  $\lambda_{\text{con}}$  for conditional gates. It is worth noting that the parameter  $\lambda$  for each element in our model is versatile with respect to the underlying hardware platform because it assumes the worst case scenario that all possible Pauli errors of the corresponding group are applied with a given error probability.

Using the total decoherence parameter,  $\lambda_{\text{tot}}$ , we can estimate a lower bound for the process fidelity of the entire circuit [14], using the following inequality

$$F_{\text{pro}} \geq e^{-\lambda_{\text{tot}}}. \quad (5)$$

This benchmark choice comes as a compromise, since for large circuits, e.g., over 10 qubits, it is practically impossible

to simulate the effect of quantum noise on classical computers and calculate the exact value of fidelity. However, this bound allows us to compare on an equal footing the impact of decoherence and draw useful conclusions.

The parameters:  $t_{\text{idle}}$ ,  $n_{\text{CX}}$ ,  $n_{\text{meas}}$ ,  $n_{\text{in}}$  and  $n_{\text{con}}$  are integer values dependent on the circuit at hand. In Table I, we present the error budget for all considered core circuits in terms of the number of register qubits  $n$ . We observe that  $t_{\text{idle}}$  scales quadratically for all unitary core circuits, as opposed to non-unitary ones which scale linearly. Given that the reverse trend is not observed for  $n_{\text{CX}}$ , there must be a regime for which non-unitary core circuits are less noisy than the corresponding unitary ones, something that is discussed in the next section.

### IV. RESULTS

From the error budget in Table I, we see that the error elements scale similarly for all three core circuits, so in this section we present the results of core 1, while the rest can be found in the Appendix E. Typically the error probability of single qubit gates is smaller than two-qubit ones, so we assume that each conditional gate has an error probability equal to  $p_{\text{con}} = p_{\text{CX}}/10$ . Following the same reasoning, we assume that the qubit initialization and measurement error probabilities are also one order of magnitude smaller than  $p_{\text{CX}}$ , i.e.,  $p_{\text{in}} = p_{\text{CX}}/10$  and  $p_{\text{meas}} = p_{\text{CX}}/10$ . We let the parameters  $p_{\text{idle}}$  and  $p_{\text{CX}}$  to span from  $1e-5$  to  $1e-3$  and  $1e-4$  to  $1e-2$ , respectively. Note that for conditional gates we assume that their decoherence is given by  $\lambda_{\text{con}} = (\lambda_{\text{idle}} + \lambda_X)/2$ , as they are not applied all the time.

In Figure 4(a) we consider the case of 50 register qubits and present two plots whose color indicates the lower bound of the process fidelity of the entire circuit, given in the right-hand side of expression (5). Note that the color bar corresponds to both of them for an easier comparison. We see that the unitary circuit performs the best for low idling error, while the opposite is true for the non-unitary circuit. In order to compare them quantitatively, we present in Figure 4(b) another plot but now the colorbar corresponds to the  $\Delta$  Fidelity, i.e., the process fidelity of the unitary circuit minus the non-unitary one. Positive values, represented with red color, imply a better performance for the unitary circuit, and negative values, represented with blue color, imply a better performance for the

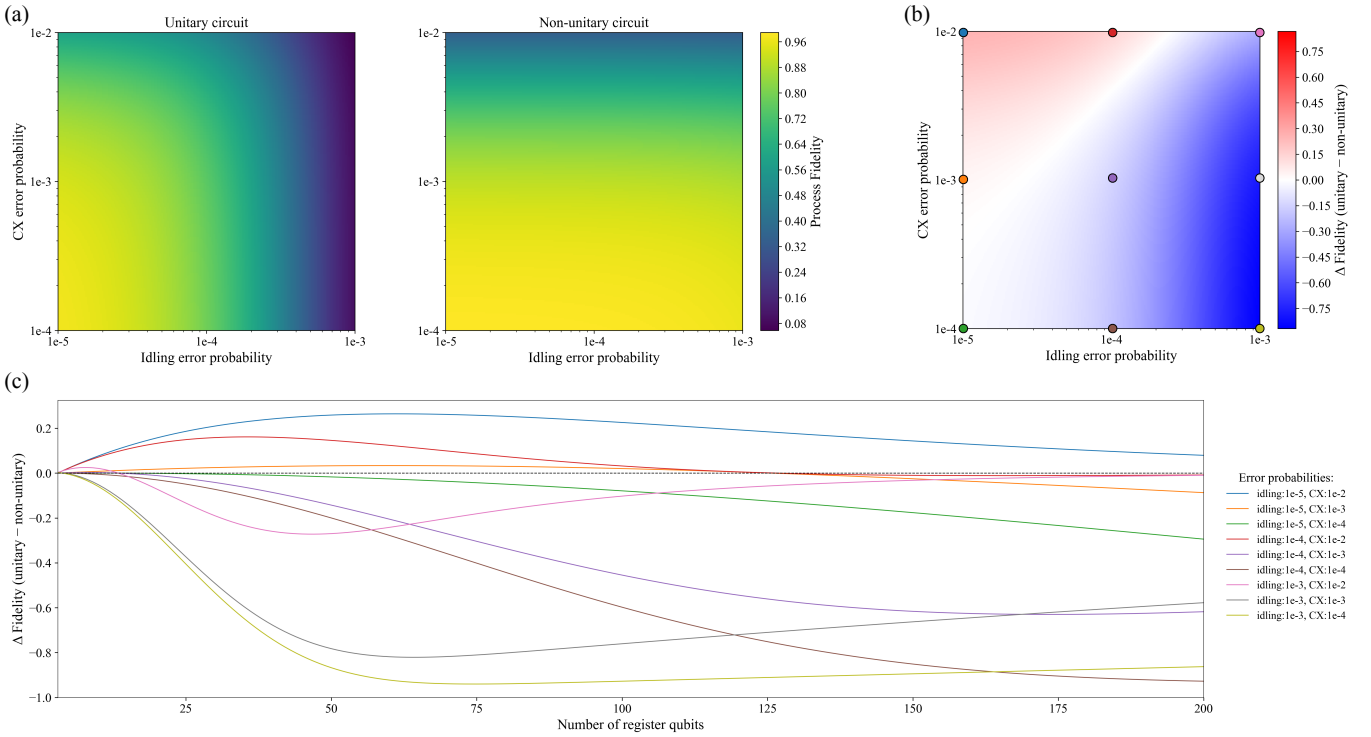


FIG. 4. In panel (a) two plots are presented for the unitary and the non-unitary version of core 1. Both have the same range in terms of idling error probability and CX error probability:  $1e-5$  to  $1e-3$  and  $1e-4$  to  $1e-2$ , respectively. The colorbar corresponds to both plots and indicates the lower bound of process fidelity of the entire circuit, which appears to be at its highest for the unitary circuit when idling error probability is low, and for the non-unitary circuit when CX error probability is low. In panel (b) the difference of the process fidelities is shown,  $\Delta$  Fidelity, where positive (red) indicates an advantage for the unitary circuit and negative (blue) for the non-unitary one. Finally, in panel (c) we present the  $\Delta$  Fidelity against the number of register qubits for nine different error probabilities, which are also indicated as colored dots on the plot of panel (b).

non-unitary ones.

In Figure 4(c) we select nine pairs for idling and CX error probabilities and plot the  $\Delta$  Fidelity against register qubits in the range up to 200. Note that for every  $n$  number of register qubits we need an extra amount of  $n - 3$  auxiliary qubits in the case of non-unitary circuits. In practice, this plot shows how Figure 4(b) evolves for different numbers of register qubits. We observe that the non-unitary construction is preferable for most of the error parameters considered in this plot, however the corresponding trends are not the same. This implies that the choice between a unitary and a non-unitary circuit should depend on the number of register qubits and the error characteristics of the platform.

## V. CONCLUSION

In summary, we have presented a method for constructing shallow depth circuits by replacing standard two-qubit entangling gates, such as the CX gate, with their measurement-based equivalent ones, corresponding to three-qubit circuits that utilize auxiliary qubits, mid-circuit measurements, and conditional single-qubit gates. This approach addresses the depth limitations imposed by finite coherence times in current

quantum hardware and is most effective for platforms where CX errors are relatively low compared to qubit idling errors. The types of circuits considered in this work are immediately relevant to VQAs, but the method used is not limited to those. Overall, the technique discussed in this work enables scalable implementation of structured circuits within the constraints of near-term devices.

## VI. ACKNOWLEDGEMENTS

This work is supported by the National Research Foundation, Singapore, and A\*STAR under its CQT Bridging Grant and by the EU HORIZON—Project 101080085 – QCFD

## Appendix A: Measurement-Based Gates

In this section we prove that the circuit in Figure 2(b) corresponds to a CX operation between the first and third qubits. We begin by considering two arbitrary states for qubit 1 and 3,  $\sum_{ij} \alpha_{ij} |i\rangle_1 |j\rangle_3$ , and a fixed state for qubit 2,  $|+\rangle_2 = (|0\rangle_2 + |1\rangle_2)/\sqrt{2}$ , so the combined input state is written as

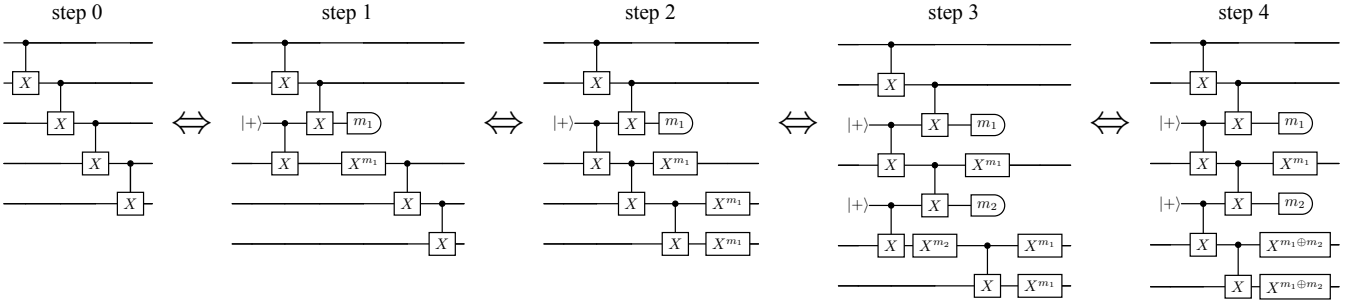


FIG. 5. Step by step transition from a unitary to a non-unitary circuit. Step 0 is the initial unitary circuit. Step 1 shows the first substitution of a CX gate with its measurement-based equivalent. In step 2 the commutation of the conditional gate takes place. In step 3 the second substitution of CX is shown. Finally, in step 4 the last gate commutation takes place.

follows:

$$|\psi_0\rangle = \frac{1}{\sqrt{2}} \sum_{ij} \alpha_{ij} |i\rangle_1 (|0\rangle_2 + |1\rangle_2) |j\rangle_3. \quad (\text{A1})$$

We, then, apply a CX gate, using qubit 2 as control and qubit 3 as target. The resulting state is

$$|\psi_1\rangle = \frac{1}{\sqrt{2}} \sum_{ij} \alpha_{ij} (|i\rangle_1 |0\rangle_2 |j\rangle_3 + |i\rangle_1 |1\rangle_2 |j \oplus 1\rangle_3). \quad (\text{A2})$$

Next, we apply a CX gate, using qubit 1 as control and qubit 2 as target:

$$|\psi_2\rangle = \frac{1}{\sqrt{2}} \sum_{ij} \alpha_{ij} (|i\rangle_1 |i\rangle_2 |j\rangle_3 + |i\rangle_1 |i \oplus 1\rangle_2 |j \oplus 1\rangle_3). \quad (\text{A3})$$

The next operation is a measurement on the second qubit, which corresponds to a projection onto the computational basis  $|m\rangle \in \{|0\rangle, |1\rangle\}$ :

$$|\psi_3\rangle = \frac{1}{\sqrt{2}} \sum_{ij} \alpha_{ij} (|i\rangle_1 |m\rangle \langle m| |i\rangle_2 |j\rangle_3 + |i\rangle_1 |m\rangle \langle m| i \oplus 1\rangle_2 |j \oplus 1\rangle_3). \quad (\text{A4})$$

For  $m = 0$  and  $m = 1$  we have respectively:

$$|\psi_3\rangle = \frac{1}{\sqrt{2}} \sum_j (\alpha_{0j} |0\rangle_1 |0\rangle_2 |j\rangle_3 + a_{1j} |1\rangle_1 |0\rangle_2 |j \oplus 1\rangle_3), \quad (\text{A5a})$$

$$|\psi_3\rangle = \frac{1}{\sqrt{2}} \sum_j (\alpha_{1j} |1\rangle_1 |1\rangle_2 |j\rangle_3 + a_{0j} |0\rangle_1 |1\rangle_2 |j \oplus 1\rangle_3), \quad (\text{A5b})$$

which can be written more compactly as

$$|\psi_3\rangle = \frac{1}{\sqrt{2}} \sum_j (\alpha_{0j} |0\rangle_1 |m\rangle_2 |j \oplus m\rangle_3 + a_{1j} |1\rangle_1 |m\rangle_2 |j \oplus m \oplus 1\rangle_3). \quad (\text{A6})$$

When the projection is equal to  $|m\rangle_1 = |0\rangle_1$ , we do not perform any other operation on the circuit, i.e.,

$$|\psi_4\rangle = \frac{1}{\sqrt{2}} \sum_j (\alpha_{0j} |0\rangle_1 |0\rangle_2 |j\rangle_3 + a_{1j} |1\rangle_1 |0\rangle_2 |j \oplus 1\rangle_3), \quad (\text{A7})$$

but when  $|m\rangle_1 = |1\rangle_1$ , we apply an X gate to the third qubit, i.e.,

$$|\psi_4\rangle = \frac{1}{\sqrt{2}} \sum_j (\alpha_{0j} |0\rangle_1 |1\rangle_2 |j\rangle_3 + a_{1j} |1\rangle_1 |1\rangle_2 |j \oplus 1\rangle_3). \quad (\text{A8})$$

Tracing out the second qubit, we arrive at

$$\begin{aligned} |\psi_5\rangle &= \sum_j (\alpha_{0j} |0\rangle_1 |j\rangle_3 + a_{1j} |1\rangle_1 |j \oplus 1\rangle_3) \\ &= \sum_{kj} \alpha_{kj} |k\rangle_1 |j \oplus k\rangle_3, \end{aligned} \quad (\text{A9})$$

which is the CX transformation on qubits 1 and 3, thus completing the proof.

The proof for the second circuit with the fixed state  $|0\rangle$  and the Z conditional gate is analogous so we omit it for brevity.

## Appendix B: Modular Construction

In Figure 5 the transition from a unitary to a non-unitary circuit is shown by substituting CX gates with their equivalent measurement-based circuit, as shown in Figure 2(b). In step 0, we have the initial unitary circuit. In step 1, we substitute the second CX gate with the circuit primitive. In step 2, we commute the rest of CX gates over the conditional gate that was introduced in the previous step. That has as a result the introduction of two more conditional gates on the last two qubits, due to the identity  $(X \otimes I)CX = CX(X \otimes X)$ . In step 3, we substitute one more CX gate with the circuit primitive, and finally in step 4, we commute the last conditional gate.

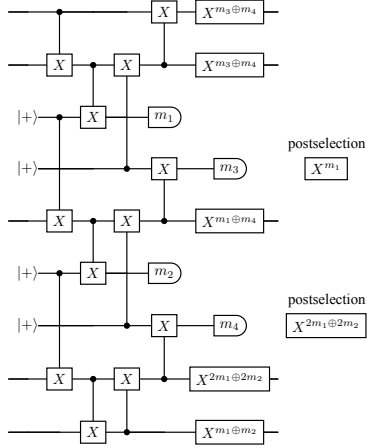


FIG. 6. Non-unitary version of core 3 circuit, with all measurements pushed at the end. By postselection we mean that the indicated gate has to be performed at the end classically.

### Appendix C: Alternative Non-Unitary Core 3

In the main text, core 3 includes a series of mid-circuit measurements. Those can be commuted to the end of the circuit, as seen in Figure 6. In this case long-range CX gates are involved that might not be easily implementable on some quantum computing platforms. The resulting circuit performs only slightly better compared to the circuit presented in the main text, but due to the long-range CX gates, it would be preferable only if the platform can efficiently implement distant CX gates, while mid-circuit measurements remain too noisy.

### Appendix D: Achieving Target State

In Table II we report the infidelities for different number of layers used in the non-unitary ansatz circuits during the optimization of variational states for the three target states. It is apparent that as more layers are employed in the simulation, the infidelity gets lower, implying a better approximation.

TABLE II. Infidelity between the simulated and target state for different numbers of layers. For all calculations we have assumed 10,000 iterations.

	Layer 1	Layer 2	Layer 3	Layer 4	Layer 5
State 1	5.1e-5	1.7e-5	8.3e-6	1.5e-6	1.5e-13
State 2	4.1e-2	3.5e-4	6.4e-9	7.8e-9	2.1e-13
State 3	7.8e-2	7.5e-3	1.7e-10	8.9e-10	5.2e-14

It is clear that for all considered core circuits the non-unitary structure offers a less noisy alternative across a wide range of register-qubit counts and error characteristics.

### Appendix E: Results for Core 2 and Core 3

In Figure 7 analogous results of Figure 4(c) are presented for core circuits 2 and 3. Qualitatively, they show a similar behavior to core 1, as all three have a similar ladder structure.

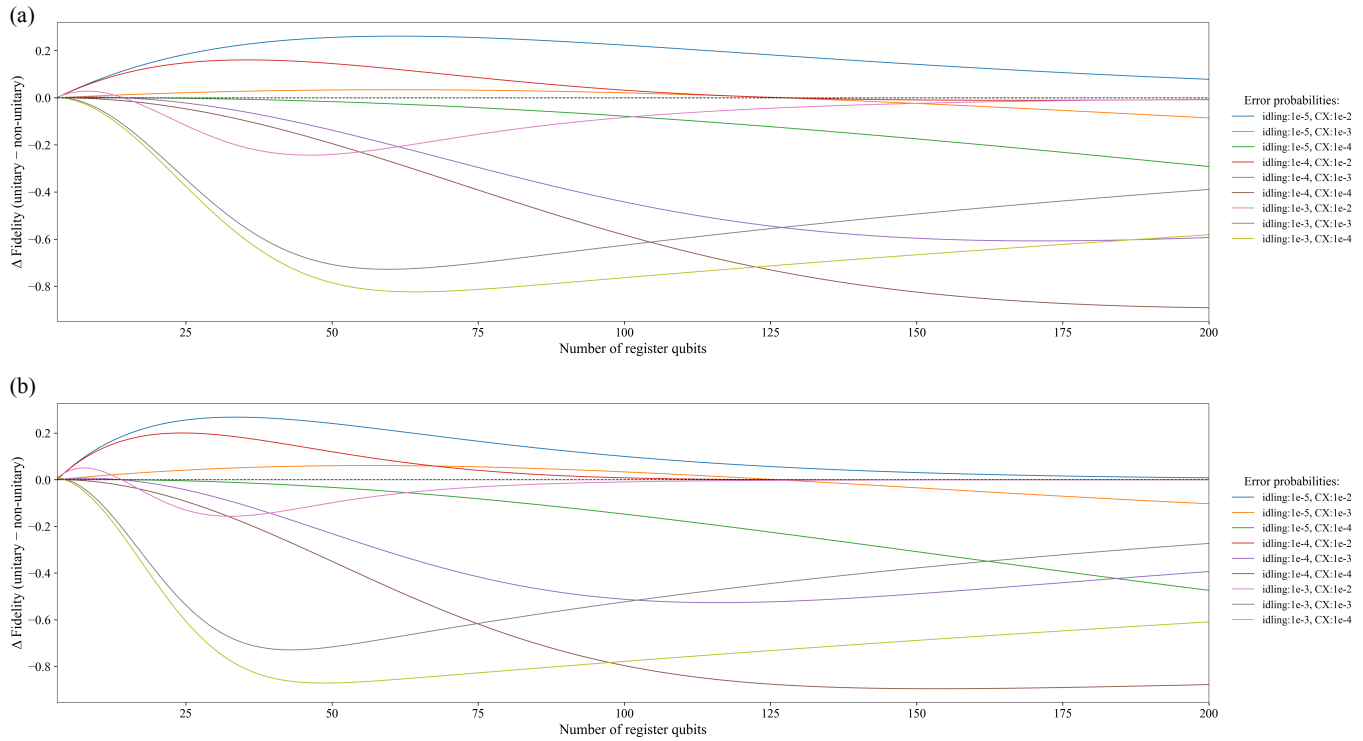


FIG. 7. In panel (a) the difference in process fidelities is shown for core 2 and in panel (b) for core 3. The different colors correspond to different sets of error probabilities indicated on the right-hand side of the figures.

[1] A. Bennakhi, G. T. Byrd, and P. Franzon, Analyzing quantum circuit depth reduction with ancilla qubits in MCX gates, in *2024 IEEE International Conference on Quantum Computing and Engineering (QCE)* (IEEE, 2024) p. 510–511.

[2] H. R. Grimsley, S. E. Economou, E. Barnes, and N. J. Mayhall, An adaptive variational algorithm for exact molecular simulations on a quantum computer, *Nature Communications* **10**, 10.1038/s41467-019-10988-2 (2019).

[3] H. L. Tang, V. Shkolnikov, G. S. Barron, H. R. Grimsley, N. J. Mayhall, E. Barnes, and S. E. Economou, Qubit-ADAPT-VQE: An adaptive algorithm for constructing hardware-efficient ansätze on a quantum processor, *PRX Quantum* **2**, 020310 (2021).

[4] Y. S. Yordanov, V. Armaos, C. H. W. Barnes, and D. R. M. Arvidsson-Shukur, Qubit-excitation-based adaptive variational quantum eigensolver, *Communications Physics* **4**, 10.1038/s42005-021-00730-0 (2021).

[5] S. Sim, J. Romero, J. F. Gonthier, and A. A. Kunitsa, Adaptive pruning-based optimization of parameterized quantum circuits, *Quantum Science and Technology* **6**, 025019 (2021).

[6] Z. Hu, P. Dong, Z. Wang, Y. Lin, Y. Wang, and W. Jiang, Quantum neural network compression, in *Proceedings of the 41st IEEE/ACM International Conference on Computer-Aided Design*, ICCAD '22 (ACM, 2022) p. 1–9.

[7] C. Moore and M. Nilsson, Parallel quantum computation and quantum codes, *SIAM Journal on Computing* **31**, 799–815 (2001).

[8] J. Anders, D. K. L. Oi, E. Kashefi, D. E. Browne, and E. Andersson, Ancilla-driven universal quantum computation, *Physical Review A* **82**, 10.1103/physreva.82.020301 (2010).

[9] T. J. Proctor, E. Andersson, and V. Kendon, Universal quantum computation by the unitary control of ancilla qubits and using a fixed ancilla-register interaction, *Physical Review A* **88**, 10.1103/physreva.88.042330 (2013).

[10] T. J. Proctor and V. Kendon, Minimal ancilla mediated quantum computation, *EPJ Quantum Technology* **1** (2014).

[11] J. Jiang, X. Sun, S.-H. Teng, B. Wu, K. Wu, and J. Zhang, Optimal space-depth trade-off of CNOT circuits in quantum logic synthesis, in *Proceedings of the Fourteenth Annual ACM-SIAM Symposium on Discrete Algorithms* (Society for Industrial and Applied Mathematics, 2020) p. 213–229.

[12] Y. Quel, E. Kaur, and M. M. Wilde, Multivariate trace estimation in constant quantum depth, *Quantum* **8**, 1220 (2024).

[13] H. Buhrman, M. Folkertsma, B. Loff, and N. M. P. Neumann, State preparation by shallow circuits using feed forward, *Quantum* **8**, 1552 (2024).

[14] E. Bäumer, V. Tripathi, D. S. Wang, P. Rall, E. H. Chen, S. Majumder, A. Seif, and Z. K. Minev, Efficient long-range entanglement using dynamic circuits, *PRX Quantum* **5**, 030339 (2024).

[15] E. Bäumer and S. Woerner, Measurement-based long-range entangling gates in constant depth, *Physical Review Research* **7**, 023120 (2025).

[16] J. E. Chenfeng Cao, Measurement-driven quantum advantages in shallow circuits, *arXiv:2505.04705* (2025).

[17] M. A. Nielsen and I. L. Chuang, Programmable quantum gate arrays, *Physical Review Letters* **79**, 321 (1997).

[18] D. Gottesman and I. L. Chuang, Demonstrating the viability of universal quantum computation using teleportation and single-

qubit operations, *Nature* **402**, 390–393 (1999).

[19] M. Cerezo, A. Arrasmith, R. Babbush, S. C. Benjamin, S. Endo, K. Fujii, J. R. McClean, K. Mitarai, X. Yuan, L. Cincio, and P. J. Coles, Variational quantum algorithms, *Nature Reviews Physics* **3**, 625–644 (2021).

[20] K. Bharti, A. Cervera-Lierta, T. H. Kyaw, T. Haug, S. Alperin-Lea, A. Anand, M. Degroote, H. Heimonen, J. S. Kottmann, T. Menke, W.-K. Mok, S. Sim, L.-C. Kwek, and A. Aspuru-Guzik, Noisy intermediate-scale quantum algorithms, *Review of Modern Physics* **94**, 015004 (2022).

[21] S. Sim, P. D. Johnson, and A. Aspuru-Guzik, Expressibility and entangling capability of parameterized quantum circuits for hybrid quantum-classical algorithms, *Advanced Quantum Technologies* **2** (2019).

[22] M. Umer, E. Mastorakis, S. Evangelou, and D. G. Angelakis, Probing the limits of variational quantum algorithms for nonlinear ground states on real quantum hardware: The effects of noise, *Physical Review A* **111**, 012626 (2025).

[23] M. Umer, E. Mastorakis, and D. G. Angelakis, Efficient estimation and sequential optimization of cost functions in variational quantum algorithms, *Quantum Science and Technology* **10**, 035022 (2025).

[24] A. Yimsiriwattana and S. J. Lomonaco Jr, Generalized GHZ states and distributed quantum computing, *arXiv:0402148* (2004).

[25] N. N. Daniel Litinski, Active volume: An architecture for efficient fault-tolerant quantum computers with limited non-local connections, *arXiv:2211.15465* (2022).

[26] M. Lubasch, J. Joo, P. Moinier, M. Kiffner, and D. Jaksch, Variational quantum algorithms for nonlinear problems, *Physical Review A* **101**, 010301 (2020).

[27] A. Uhlmann, The “transition probability” in the state space of a  $*$ -algebra, *Reports on Mathematical Physics* **9**, 273–279 (1976).

[28] R. Jozsa, Fidelity for mixed quantum states, *Journal of Modern Optics* **41**, 2315–2323 (1994).

[29] E. van den Berg, Z. K. Minev, A. Kandala, and K. Temme, Probabilistic error cancellation with sparse Pauli–Lindblad models on noisy quantum processors, *Nature Physics* **19**, 1116–1121 (2023).